Nano Research

ISSN 1998-0124 CN 11-5974/O4
https://doi.org/10.1007/s12274-021-3473-1

Research Article

Epitaxially aligned single-crystal gold nanoplates formed in large-area arrays at high yield

Trevor B. Demille[1,§], Robert D. Neal[1,§], Arin S. Preston[1], Zijuan Liang[1], Allen G. Oliver[2], Robert A. Hughes[1], and Svetlana Neretina[1,2] (✉)

[1] *College of Engineering, University of Notre Dame, Notre Dame, Indiana 46556, USA*
[2] *Department of Chemistry and Biochemistry, University of Notre Dame, Notre Dame, Indiana 46556, USA*
[§] *Trevor B. Demille and Robert D. Neal contributed equally to this work.*

Received: 12 February 2021 / **Revised:** 24 March 2021 / **Accepted:** 25 March 2021

ABSTRACT

Well-tailored nanomaterials with a single-crystal character provide ideal building blocks for on-chip plasmonic devices. Although colloidal methods have demonstrated mastery over the synthesis of such structures, it has proven quite difficult to deploy these same nanomaterials on substrate surfaces in a highly deterministic manner where precise control over position and orientation is ensured. Herein, we demonstrate a room-temperature two-reagent liquid-phase seed-mediated synthesis of gold nanoplates directly on substrate surfaces in arrays over a square-centimeter area. The synthesis is reliant on benchtop lithographic and directed-assembly processes that give rise to single-crystal seeds of gold that express both an epitaxial relationship with the underlying substrate and the internal defect structure required to promote a two-dimensional growth mode. The resulting structures are highly faceted and, because seed-substrate epitaxy is imposed upon the growing nanoplates, are identically aligned on the substrate surface. Nanoplate yields are increased to values as high as 95% using a post-processing sonication procedure that selectively removes a small population of irregularly shaped nanostructures from the substrate surface, and in doing so, gives rise to an uncompromised plasmonic response. The work, therefore, advances the techniques needed to integrate single-crystal nanomaterials with wafer-based technologies and provides leading-edge capabilities in terms of defining large-area arrays of plasmonic structures with the nanoplate geometry.

KEYWORDS

nanoplates, epitaxial, array, plasmon, Brij-700 block copolymer, substrate

1 Introduction

The integration of single-crystal nanomaterials with large-area wafer-based processing technologies remains a grand challenge whose resolution would provide a device-quality platform with tailorable properties. Within this domain, plasmonic nanometals offer compelling opportunities in terms of fabricating photo- and chemically-active surfaces whose functionality benefits from the collective response derived from the organized placement of rationally designed nanostructures. With colloidal syntheses providing exacting controls over nanostructure size, shape, and composition and lithographic processes providing avenues for deterministic positioning, the two essential ingredients are largely in place; however, their union into a viable technology that answers to the requirements of functionality, scalability, throughput, and cost-effectiveness remains a daunting challenge [1, 2]. Rapid advances are, however, occurring as emerging techniques such as DNA-assisted assembly [3, 4], colloidal assembly [5, 6], seed-mediated syntheses [7], electrostatic assembly [8, 9], polymer-mediated synthesis [10, 11], optical printing [12], and electrophoretic deposition [13] continue to push the envelope on what is considered to be leading edge capabilities.

Noble metal nanoplates represent a remarkable class of nanostructures [14, 15] that provide a highly compatible geometry for integration with wafer-based processing because the combination unites two systems that have an inherently two-dimensional character. As such, numerous routes have been used to generate substrate-based noble metal nanoplates through their synthesis directly on a substrate [16–21] or by synthesizing a colloid that is then applied to a substrate [3, 22–30]. Stemming from this work is a broad range of potential applications including chemical [22, 31] and biological sensing [26, 32, 33], catalysis [34, 35], reconfigurable plasmonics [3], and nano-electronics [36]. Nevertheless, there exist relatively few examples where plasmonic nanoplates have been arranged into organized configurations. Progress has, however, been made in assembling close-packed configurations of triangular nanoplates using techniques such as air–liquid interfacial assembly [22–24] or solvent evaporation assembly [25–27]. Only three examples currently exist in the literature where standalone single-crystal noble metal nanoplates have been formed on substrate surfaces in periodic arrays. These demonstrations, while impressive, are deficient in that they have either been demonstrated over small areas that are less than a square-millimeter [3, 28] or on a square-centimeter length-scale but where the nanoplate yield is unsatisfactory [16].

Our group has forwarded a strategy for the nanofabrication

Address correspondence to sneretina@nd.edu

of periodic arrays of noble metal nanostructures in which single-crystal seed arrays are fabricated using nanoimprint lithography in combination with directed assembly and then transformed into complex architectures using liquid-phase syntheses adapted from well-established colloidal chemistries [7, 37]. The application of this approach to nanoplate geometries is, however, complicated by the fact that their growth in liquid media requires seeds with stacking fault defects that act as symmetry-breaking structures able to promote a two-dimensional growth mode in an otherwise isotropic metal [38, 39]. If planar growth is to occur parallel to the substrate, then it places further requirements on the seeds in that they must have their [111]-axes normal to the substrate surface where stacking faults exist along these axes but not along the equivalent $[\bar{1}11]$-, $[1\bar{1}1]$-, and $[11\bar{1}]$ axes. In prior work, we demonstrated that such seeds could be fabricated at a 78% yield but the Au nanoplates produced showed a plasmonic response that was corrupted by a population of three-dimensional structures that occupied other available sites [16]. Also disadvantageous was that the nanoplate synthesis was complicated by the use of a plasmon-mediated growth mode requiring parametric controls based on the light source used. Herein, we present a straightforward two-reagent room-temperature synthesis that when practiced on periodic arrays of substrate-based seeds yields Au nanoplates at high-yield over large areas. With unwanted three-dimensional structures selectively removed through a post-synthesis procedure, the remaining substrate-based structures collectively display the plasmonic response that is intrinsic to the nanoplate geometry.

2 Results

2.1 Nanoplate synthesis

Substrate-based Au nanoplates were prepared using a synthetic strategy [7, 37] in which lithographic techniques, in combination with vapor phase assembly processes, were used to fabricate periodic arrays of Au nanostructures that were then exposed to a liquid-phase chemical environment capable of promoting a seed-mediated growth mode yielding highly faceted planar morphologies. For nanoplate growth, seed preparation is crucial in that it must yield nanostructures with stacking fault defects running parallel to the surface of the substrate so as to provide a break in crystal symmetry able to promote two-dimensional growth. Such seeds were prepared in periodic arrays over 1 cm^2 areas using procedures described in detail elsewhere [16]. The overall process is one where nanoimprint lithography is used to define arrays of Au-capped Sb discs that, when heated, assemble into crystalline Au nanostructures. The Sb is sacrificial but where its presence is crucial in that it promotes the assembly of Au as it sublimates [40]. Figure 1(a) shows the SEM image of a Au seed array where the seeds have a roundish morphology with an average diameter of 70 nm. Significant is that the Au seeds are [111]-oriented and share a heteroepitaxial relationship with the underlying [0001]-oriented sapphire substrate [16].

Once fabricated, the seeds are subjected to a two-reagent solution-based growth mode where $HAuCl_4$ acts as the metal precursor and Brij-700 plays the dual role of shape-directing and reducing agent. It should be noted that Brij-700 has been used in this capacity in numerous noble metal syntheses [41–44]. The synthesis, which is shown schematically in Fig. 1(b), sees the Au seed array placed face-up at the bottom of a reaction vessel containing 10.8 mL of 6.8 mM aqueous Brij-700 and stirred. Growth is then initiated by the rapid addition of 1.2 mL of 10 mM aqueous $HAuCl_4$, an addition that causes the growth solution to become a slightly cloudy yellow hue. The final molarity of Brij-700 and $HAuCl_4$ under optimized conditions is, therefore, 5 and 1 mM, respectively. Syntheses are typically allowed to continue for 2 to 6 h under continuous stirring. The growth solution shows no significant color change over the course of the synthesis apart from its yellow color becoming somewhat fainter as the Au^{3+} ions are consumed. The lack of a significant color change also indicates that the spontaneous nucleation of colloidal structures is highly unfavorable. At the end of the synthesis, the sample is removed, rinsed with deionized (DI) water and isopropanol, and sonicated in DI water to remove any remaining Brij-700.

Figures 1(c) and 1(d) show both low- and high-magnification SEM images of a Au nanoplate array. The low magnification

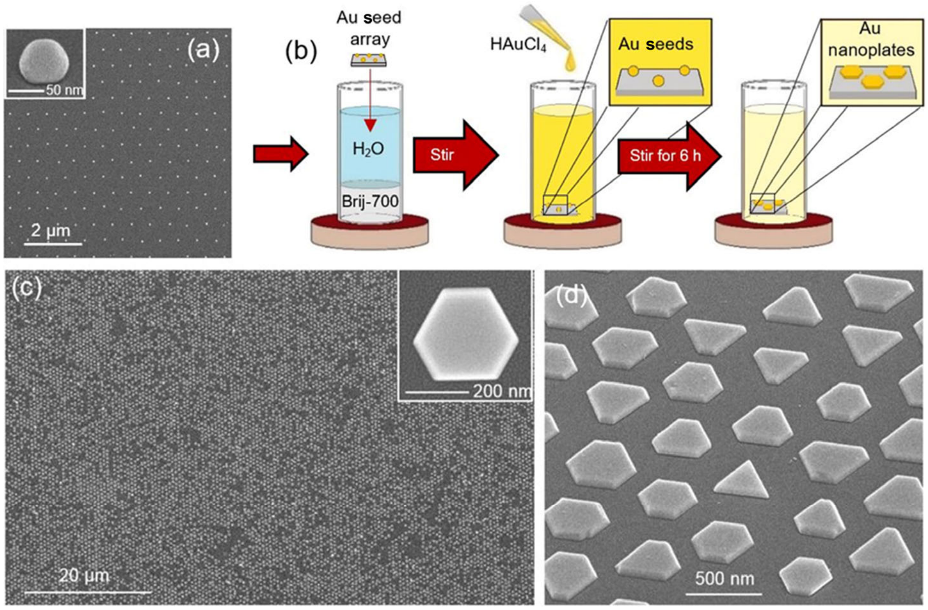

Figure 1 (a) SEM image of a periodic array of Au nanostructures that act as seeds for nanoplate growth. (b) Schematic representation of the solution-based Brij-700-directed nanoplate growth mode. (c) Low-magnification SEM image of a nanoplate array where the inset shows a top-view perspective of an individual structure. (d) Tilted-view image of nanoplates where neighboring structures exhibit parallel side-faceting due to a heteroepitaxial relationship between the Au seed and sapphire substrate.

image reveals an array with many imperfections in the form of missing structures. Although nanoimprint lithography is prone to such imperfections as the stamp wears, the sheer number of missing structures invalidates this explanation, a conclusion corroborated by the relative perfection observed in the seed array (Fig. 1(a)). A closer inspection of the arrayed structures reveals that nearly all of them are nanoplates (Fig. S1 in the Electronic Supplementary Material (ESM)). This result is in stark contrast to our prior work [16] where similarly fabricated seeds, when exposed to a light-mediated Au nanoplate synthesis, gave rise to arrays with few missing structures but where the nanoplate yield was only 78%. The remaining 22% of structures have a three-dimensional character due to a significant population of seeds having an internal defect structure that is inconsistent with the planar growth mode. The comparison suggests that these three-dimensional structures are unable to survive the processing conditions used. The nanoplate structures themselves can express a hexagonal, triangular, or corner-truncated triangular geometry. The structures have a radial extent that ranges from 200 to 400 nm with a thickness of approximately 70 nm where the edges are tapered due to faceting. Also noteworthy is that the faceting of individual structures is quite pronounced where neighboring nanoplates show identical in-plane alignment relative to each other (Fig. 1(d)), a property derived from the seed-substrate heteroepitaxial relationship being imposed onto the growing nanoplate.

Nanoplate-substrate heteroepitaxy was further assessed using X-ray diffraction (XRD) pole figure analysis. Such measurements more accurately gauge nanostructure–substrate heteroepitaxy as they probe the entire substrate surface as opposed to a select group of structures observed in transmission electron microscopy (TEM) studies. Simply stated, a pole figure is a stereographic projection that maps the real space directions (i.e., poles) where a specific crystallographic (*hkl*) periodicity lies. If, for example, a (111) pole figure shows a pole at its center, then it indicates that a <111>-direction is normal to the substrate surface. If, instead, it lies at the perimeter of the pole figure, then a <111>-direction is parallel to the substrate surface. Intermediate values indicate that a <111>-direction is a set value between these two extremes. A Au single-crystal with its [111]-axis normal to the substrate will, hence, exhibit a pole figure with a central [111] pole surrounded by $[\bar{1}11]$, $[1\bar{1}1]$, and $[11\bar{1}]$ poles forming a three-fold symmetric ring because the symmetry of the fcc crystal structure demands that these equivalent crystallographic directions emerge from the substrate surface at an angle of 70.5° from the normal.

Two pole figures were generated corresponding to the Au <111> and sapphire $<02\bar{2}4>$ reflections (Figs. 2(a) and 2(b)). The Au <111> pole figure exhibits an intense central pole surrounded by six less intense poles that form a six-fold symmetric ring at 70.5°. The fact that there are six peaks in the outer ring instead of three is significant in that it shows that the Au nanoplates, while all having their [111]-axis normal to substrate surface, express two equivalent in-plane orientations offset by 180°. The existence of two equally probable in-plane orientations has its origins in two separate effects. The first stems from the fact that [111]-oriented Au nanoplates can have either an ABCABC... stacking order or the reverse ACBACBA... stacking order, neither of which has an advantage in terms of epitaxy. This difference, however, leads to a 180° in-plane rotation of all crystallographic axes relative to the underlying substrate (Fig. 2(c)) [45]. Likewise, any nanoplate with a twin plane parallel to the substrate surface will invert the stacking order and contribute to both sets of peaks. The sapphire $<02\bar{2}4>$ pole figure shows a three-fold symmetric ring consisting of three poles at 59.5° from the normal that correspond to its $[02\bar{2}4]$, $[\bar{2}024]$, and $[2\bar{2}04]$ reflections. With the position of these poles relative to those in the Au [111] pole figure defined, it is possible to infer the two Au–sapphire orientational relationships as $(111)[\bar{2}11]$Au ∥ $(0001)[11\bar{2}0]$ sapphire and $(111)[2\bar{1}\bar{1}]$Au ∥ $(0001)[11\bar{2}0]$ sapphire. Additional data in the form of a Bragg–Brentano θ–2θ scan (Fig. S2 in the ESM), yields the anticipated Au(111) *d*-spacing of 2.3546 Å, further confirming nanoplate crystallinity.

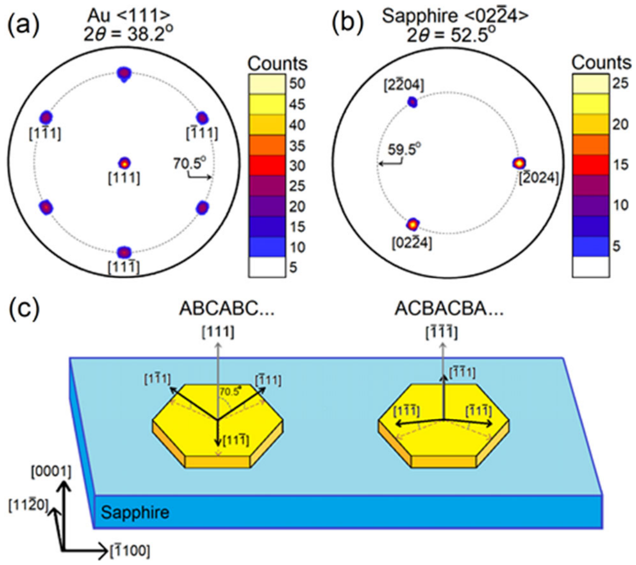

Figure 2 XRD pole figures for (a) Au <111> and (b) sapphire $<02\bar{2}4>$ reflections obtained for an array of Au nanoplates sharing a heteroepitaxial relationship with a [0001]-oriented sapphire substrate. (c) Schematic showing the two possible epitaxial relationships the Au nanoplate can have with the sapphire substrate.

2.2 Parametric controls for the nanoplate growth mode

The optimized growth conditions used to prepare the Au nanoplates shown in Figs. 1(c) and 1(d) are the product of numerous syntheses in which key parameters, such as the growth time, reactant concentrations, pH, temperature, and degree of illumination are varied. Although syntheses are typically allowed to occur for durations lasting 4 to 6 h, the radial expansion of the nanoplates shows no signs of abating with time. In fact, prolonged syntheses lead to the collision and often seamless merger of adjacent nanoplates (Fig. S3 in the ESM). This finding is not unexpected given that the growth proceeds in the absence of colloidal growth, and as a result, there is no competition for the available reactants. Moreover, substrate-based nanometal growth modes carried out in liquid media can use reactant concentrations that are far in excess of what can reasonably be consumed in the reaction occurring on the substrate surface. To illustrate this point, it is noted that if all the Au atoms introduced into this synthesis were to be deposited on the substrate surface, then it would lead to a continuous Au film with a thickness of 1.2 μm. With Brij-700 being introduced at even higher molarity, it too is similarly oversupplied. Therefore, the reaction is terminated not by the consumption of reactants but by the removal of the substrate from the growth solution.

Variations to the final Brij-700 concentration ranging from 3 to 7 mM indicate a loss of size uniformity at both extremes of this range. Low molarity values lead to numerous structures having a more three-dimensional character whereas high values consistently show planar structures but where the range in nanoplate diameters express a rather broad size distribution (Fig. S4 in the ESM). At both extremes, the nanoplate growth rate has a rather large structure-to-structure variation. Variations to the final HAuCl$_4$ concentration ranging from 0.3 to 3 mM indicate nanoplate evolution for all cases but where both the lower and upper extents of this range give rise to planar morphologies with irregular shapes, a failing that is far more acute for low molarities (Fig. S5 in the ESM). The nanoplate growth rate is also significantly impacted as the HAuCl$_4$ concentration is increased, showing a ten-fold increase in nanoplate area for a 6 h synthesis over the range of concentrations studied.

Given that HAuCl$_4$ not only decides the starting concentration of aqueous Au^{3+} ions but also sets the pH of the solution, a series of syntheses were carried out in which the pH was varied as the HAuCl$_4$ concentration was held constant. The pH of the starting reactants was either raised or lowered through the addition of NaOH or HCl. It is determined that there exists a broad window in pH values, extending from 3 to 11, that are amenable to nanoplate formation. Low pH values, which lie outside of this window, result in the formation of plate-like structures that grow rapidly but where their shape is often irregular or compromised by three-dimensional protrusions (Fig. S6(a) in the ESM). High pH values that fall outside the window result in near-negligible growth, leading to seed-like structures with somewhat enhanced faceting (Fig. S6(b) in the ESM).

To gain a more detailed understanding of the influence of pH within the established window, nanoplate growths were carried out at pH values of 3, 7, and 11 where the synthesis was halted at 1 h intervals to allow for the intermittent measurement of the extinction spectra. For these measurements, the sample was removed from the growth solution, quickly rinsed in DI water and isopropanol, and dried under a N$_2$ gas flow. Samples were only exposed to sonication at the conclusion of the 6 h synthesis. Control samples that did not undergo the removal and reinsertion process were used to confirm that the growth mode was not adversely influenced by these intermittent stoppages in the synthesis. Figure 3 shows the time-dependent extinction spectra for the three pH values studied as well as SEM images and the corresponding histogram of nanoplate diameters. All three syntheses show a similar trend in their extinction spectra, initially showing a weak localized surface plasmon resonance (LSPR) peak that is derived from the seeds that gains in strength as it red shifts to higher values as the growth proceeds. The latter stages of the growth are also characterized by the emergence of a broad shoulder at lower wavelengths. A closer inspection reveals that the rate at which the peak red shifts decreases as the pH increases. A similar trend is observed in the LSPR, showing a peak wavelength after 5 h at 952, 937, and 922 nm for pH values of 3, 7, and 11, respectively. This data is consistent with the SEM images in that they show a progression in nanoplate sizes that decrease as the pH increases. The 6 h spectrum for the pH 11 sample is distinct in that it is considerably broader and somewhat skewed. The breadth of the peak is consistent with a much broader nanoplate size distribution than is exhibited by the other samples. Once broadened, the peak becomes more susceptible to distortions caused by the shoulder, an influence that leads to its skewed appearance.

In our prior work [16], in which a light-mediated growth mode gave rise to an array of Au nanoplates interspersed with three-dimensional nanostructures, extinction spectra were obtained that have the same overall appearance as those shown in Figs. 3(a)–3(c). Simulations based on the discrete dipole approximation (DDA) were used to assign the LSPR peak to the nanoplates while the low wavelength shoulder was attributed to the three-dimensional structures. The implication of these findings is that three-dimensional structures also emerge in the Brij-700-based nanoplate growth mode and that the loss of these structures occurs only when the sample is subjected to a final cleaning procedure in which it is sonicated for 10 s in DI water. In an effort to validate this hypothesis, a nanoplate synthesis was carried out in which a seed array was cut in half followed by the side-by-side growth of nanoplates within the same solution. At the end of the synthesis, one piece was gently rinsed while the other underwent sonication. Figure 4(a) shows the SEM image of the gently rinsed sample that shows a full array composed of both nanoplates and three-dimensional nanostructures (circled in red). In sharp contrast, the sonicated sample (Fig. 4(b)) shows an incomplete array where the majority of surviving nanostructures exhibit the desired nanoplate geometry. In fact, a statistical analysis reveals a 95% nanoplate shape-purity after sonication. Spectroscopic characterization of a gently rinsed sample before and after sonication reveals that the high wavelength peak at 960 nm is nearly unaffected by the sonication process while the low wavelength shoulder that extends from 550 to 650 nm is dramatically weakened (Fig. 4(c)). The results provide convincing evidence that sonication acts to preferentially rid the array of undesirable three-dimensional structures.

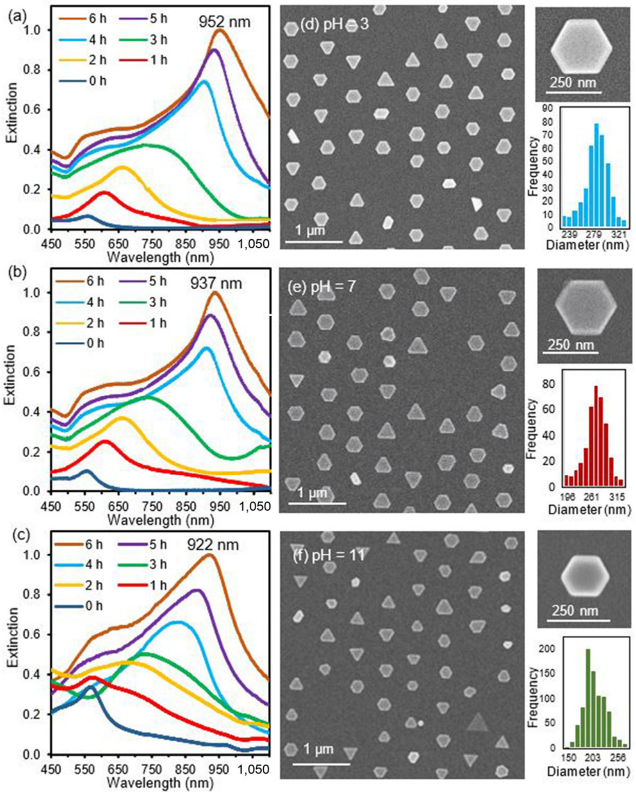

Figure 3 Time series of the extinction spectra for Au nanoplate syntheses carried out at starting pH values of (a) 3, (b) 7, and (c) 11. SEM images of the resulting nanoplates and a corresponding histogram of the nanoplate size distribution for pH values of (d) 3, (e) 7, and (f) 11. The histograms values denote the major axis diameters of the nanoplates.

Studies were also undertaken to determine whether the current Brij-700-based growth is influenced by light. Au nanoplates were, hence, grown in the absence and presence of light where the samples, in a manner analogous to the pH studies, were intermittently removed from the growth solution to measure the time dependence of the extinction spectrum (Fig. 5). The data clearly shows that illumination under an

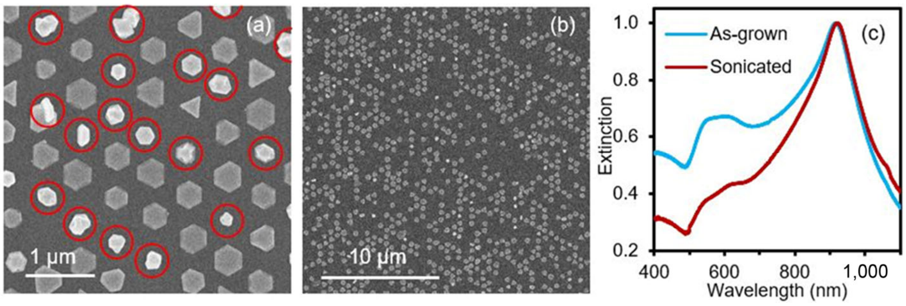

Figure 4 SEM images showing a nanoplate array after a post-synthesis procedure in which it is (a) gently rinsed and (b) gently rinsed and sonicated. (c) Extinction spectra comparing the plasmonic response of an as-grown array that was gently rinsed and the same array after undergoing sonication.

LED light source causes a much more rapid growth rate. This synthesis also distinguishes itself in that colloidal growth occurs simultaneously. In an effort to gain insights into the mechanisms by which the growth is accelerated, measurements were carried out in the dark at the somewhat elevated temperatures of 30, 40, and 50 °C (Fig. S7 in the ESM). They show that increased temperature causes a rapid increase in the growth rate followed by a rapid decline that is attributable to a competition for reactants caused by the buildup of a dense colloid. This high sensitivity to temperature points toward plasmonic heating [46] as being the dominant mechanism by which the growth rate is enhanced under illumination.

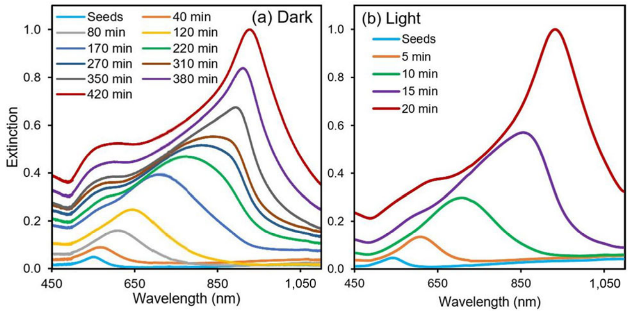

Figure 5 Time series of the extinction spectra for Au nanoplate syntheses carried out (a) in the dark and (b) under illumination.

3 Discussion

The current work presents a large-area substrate-based synthesis that is unique in that it yields a population of heteroepitaxially aligned Au nanoplates at a yield of 95%. Although the seed formation process is somewhat involved, the nanoplate synthesis itself is a simple two-reagent aqueous synthesis that can be carried out at room temperature. Variations to readily accessible growth parameters reveal that, while changes to the growth rate occur, the nanoplate formation is quite robust to substantial changes to reactant concentrations, pH, temperature, and illumination conditions. These parametric studies also show that the most favorable growth conditions are those that do not lead to spontaneous nucleation processes within the growth solution. As such, somewhat higher growth temperatures (i.e., < 40 °C) provide the best means for increasing the growth rate while maintaining the integrity of the synthesis. The synthesis is also advantageous in that nanoplate growth is not adversely affected by a process that sees the sample removed from the growth solution, optically characterized, and then reinserted back into the growth solution, a characteristic that could be used to accurately tune the LSPR to a desired value. Additionally, the procedure in which samples are sonicated to remove unwanted three-dimensional structures is beneficial in that it rids the sample of structures that corrupt the plasmonic responses from the nanoplates. Additionally, the procedure in which samples are sonicated to remove unwanted three-dimensional structures is beneficial in that it rids the sample of structures that corrupt the plasmonic response from the nanoplates. This is of significance because three-dimensional structures have been shown to negatively impact nanoplate sensing modalities based on the refractive index sensitivity of the LSPR [29, 47]. At the same time, the final product is lacking if a truly periodic array is desired because many array positions are left vacant. The resulting array is, hence, best described as having long-range order but where there exist many vacancy defects. The underlying problem, however, does not lie with the sonication step but with a seed formation process that gives rise to structures that do not have the internal defect structure needed to promote the nanoplate growth mode [16]. Advancements in seed fabrication are therefore needed.

Shape-purification of the reaction product is an interesting and significant aspect of this work, but it is by no means the first substrate-based synthesis to forward such a strategy. In some of the earliest seed-mediated liquid-phase syntheses using substrate-immobilized seeds, Zamborini and co-workers [29, 48] showed that the nanoplate yield can be increased from 44% to 90% using a post-growth sonication procedure. The literature also shows that adhesive attachment followed by stripping can also be effective in this regard [29, 31, 48, 49]. Although prior studies have reported that nanoplates remain firmly attached during sonication while more three-dimensional nanostructures do not, the underlying mechanisms are not thoroughly understood or explained. The sonication of the liquid media subjects the surface-immobilized structures to a series of rapid expansion and compression wavefronts that can even result in cavitation [50]. Nanoplates more effectively resist such forces because they possess a greater contact area with the substrate. Their two-dimensional geometry also provides benefit in that any lateral forces will exert a greater torque on a three-dimensional structure due to its considerably longer moment arm. Thus, when a three-dimensional structure experiences a torque, its removal from the surface is likely through a peeling action where bonds are sequentially broken whereas a two-dimensional object experiences more of a shear force where detachment requires nearly all of the bonds to be broken at once. It is unlikely that the degree of nanostructure adhesion is associated with the initial seed from which it is derived since the entire seed array is able to undergo prolonged sonication without the significant loss of structures.

4 Conclusions

We have demonstrated the nanofabrication of substrate-immobilized single-crystal Au nanoplates over large areas using lithographic methods in combination with a two-reagent liquid-phase seed-mediated synthesis. By taking advantage of seed-substrate epitaxy and a post-synthesis shape-purification process, nanoplates are formed at high yield with a high degree of in-plane alignment. The liquid-phase synthesis is highly advantageous in that it is not only facile but offers wide processing windows that are able to obtain the desired geometry. The work, therefore, advances the techniques and knowhow for defining organized surfaces of nanocrystals and forwards the use of Au nanoplates as an innovative building block for on-chip plasmonic devices.

5 Methods

5.1 Chemicals and materials

The target used to sputter deposit Au was cut from a 0.25 mm thick foil with 99.9985% purity (Alfa Aesar) to a 19 mm diameter. The Sb target was cut to a similar size from a rod of 99.999% purity (ESPI Metals). Two-side polished [0001]-oriented sapphire substrates, with dimensions of 10 mm × 10.5 mm × 0.65 mm, were cut from 100 mm wafers (MTI Corp.). Nanoimprint lithography stamps and the associated moldable resist were obtained from Lightsmyth Technologies and Micro Resist Technology GmbH, respectively. The high temperature directed assembly of Au seeds was carried out in ultrahigh purity Ar gas. Nanoplate syntheses utilized Brij-700 block copolymer (Spectrum Chemicals), hydrogen tetrachloroaurate(III) trihydrate ($HAuCl_4 \cdot 3H_2O$), (99.99% purity, Alfa Aesar), sodium hydroxide (NaOH, MilliporeSigma), hydrochloric acid (HCl, MilliporeSigma), and nitric acid (HNO_3, Alfa Aesar). DI water with a resistivity of 18.2 MΩ·cm was used for the preparation of all aqueous solutions.

5.2 Au seed fabrication

Periodic arrays of seeds were formed using nanoimprint lithography in combination with a high temperature directed-assembly process. Substrates were spin-coated with a 400 nm thick resist followed by a nanoimprinting procedure that embossed a hexagonal array of cylindrical holes (diameter = 240 nm, center-to-center distance = 600 nm, depth = 350 nm) over an 8 mm × 8.3 mm area. Reactive ion etching was then used to thin the patterned resist until the substrate was exposed at the bottom of each cylinder. Sb (12 nm) and Au (2.5 nm) layers were then deposited over the entire surface followed by a liftoff procedure that removed the resist as well as the Au and Sb on its surface to leave an array of Au-coated Sb discs on the substrate surface. These discs were then heated to 1,025 °C, causing them to assemble into the crystalline Au seeds shown in Fig. 1(a). Additional details regarding seed formation can be found elsewhere [16].

5.3 Au nanoplate syntheses

The optimum conditions for nanoplate synthesis saw the seed array immersed in a 30 mL beaker containing 10.8 mL of 6.8 mM aqueous Brij-700. The substrate sat face-up at the bottom beaker where it was positioned off to one side to provide room for a magnetic stirrer rotating at 300 rpm. The room temperature synthesis was then initiated by rapidly injecting $HAuCl_4$ (1.2 mL, 10 mM) and allowed to continue for times between 2 and 6 h. The reaction was terminated by removing the sample from the beaker after which it was rinsed in DI water and isopropyl alcohol and then sonicated for 10 s in DI water while holding the substrate firmly with tweezers. The sample was then dried in a N_2 gas flow. Crucial to obtaining a colloid-free synthesis is a beaker cleaning procedure that sees them sequentially exposed to boiling water and room-temperature *aqua regia* (Hazard: *aqua regia* is highly toxic and corrosive). Standard syntheses were carried out under ambient lighting. The syntheses used to obtain the data in Fig. 5(a) and Fig. S6 in the ESM were, however, carried out in the dark while those used to obtain Fig. 5(b) were carried out with an LED source (Lohas LED, 2,500 lumens, 5,000 K) with a bulb-to-sample distance of 15 cm.

5.4 Instrumentation and characterization

The seed fabrication process used a home-built nanoimprint lithography press [37] and a SAMCO RIE-1C reactive ion etcher. SEM images were obtained using a Magellan 400 FEI field emission scanning electron microscope with a secondary electron detector operating in immersion mode. XRD pole figure analysis utilized a Bruker D8 Advance diffractometer with a Vantec-500 multi-wire detector equipped with a quarter-circle Eulerian cradle. The measurements utilized a 1 mm Cu Kα X-ray point source with sample-to-detector distance of 199.3 mm. Data was collected at tilt angles (ψ) of 0°, 35°, and 70° from the horizontal using the area detector. Azimuthal angles (φ) with respect to the substrate normal were incremented by 5° per frame with a collection time of 30 s. Pole figures were generated using the open-source XRD2DScan software package [51]. The Bragg–Brentano θ–2θ XRD scan was also carried out on a Bruker D8 Advance diffractometer. Extinction spectra were acquired using a Jasco V-730 spectrophotometer.

Acknowledgements

This work is supported by the National Science Foundation Award to S.N. (No. CMMI-1911991). It has also benefited from the facilities available through the Notre Dame Molecular Structure Facility (MSF) and the Notre Dame Integrated Imaging Facility (NDIIF).

Electronic Supplementary Material: Supplementary material (additional SEM characterization of Au nanoplates synthesized under various experimental conditions) is available in the online version of this article at https://doi.org/10.1007/s12274-021-3473-1.

References

[1] Zhang, H. Y.; Kinnear, C.; Mulvaney, P. Fabrication of single-nanocrystal arrays. *Adv. Mater*. **2020**, *32*, 1904551.

[2] Hughes, R. A.; Menumerov, E.; Neretina, S. When lithography meets self-assembly: A review of recent advances in the directed assembly of complex metal nanostructures on planar and textured surfaces. *Nanotechnology* **2017**, *28*, 282002.

[3] Lin, Q. Y.; Mason, J. A.; Li, Z. Y.; Zhou, W. J.; O'Brien, M. N.; Brown, K. A.; Jones, M. R.; Butun, S.; Lee, B.; Dravid, V. P. et al. Building superlattices from individual nanoparticles via template-confined DNA-mediated assembly. *Science* **2018**, *359*, 669–672.

[4] Zhou, W. J.; Liu, Z. Z.; Huang, Z. Y.; Lin, H. X.; Samanta, D.; Lin, Q. Y.; Aydin, K.; Mirkin, C. A. Device-quality, reconfigurable metamaterials from shape-directed nanocrystal assembly. *Proc. Natl. Acad. Sci. USA* **2020**, *117*, 21052–21057.

[5] Ni, S. B.; Isa, L.; Wolf, H. Capillary assembly as a tool for the heterogeneous integration of micro- and nanoscale objects. *Soft Matter* **2018**, *14*, 2978–2995.

[6] Flauraud, V.; Mastrangeli, M.; Bernasconi, G. D.; Butet, J.; Alexander, D. T. L.; Shahrabi, E.; Martin, O. J. F.; Brugger, J. Nanoscale topographical control of capillary assembly of nanoparticles. *Nat. Nanotechnol*. **2017**, *12*, 73–80.

[7] Neretina, S.; Hughes, R. A.; Gilroy, K. D.; Hajfathalian, M. Noble metal nanostructure synthesis at the liquid–substrate interface: New

structures, new insights, and new possibilities. *Acc. Chem. Res.* **2016**, *49*, 2243–2250.

[8] Kinnear, C.; Cadusch, J.; Zhang, H. Y.; Lu, J. N.; James, T. D.; Roberts, A.; Mulvaney, P. Directed chemical assembly of single and clustered nanoparticles with silanized templates. *Langmuir* **2018**, *34*, 7355–7363.

[9] Yang, L. L.; Yan, B.; Premasiri, W. R.; Ziegler, L. D.; Dal Negro, L.; Reinhard, B. M. Engineering nanoparticle cluster arrays for bacterial biosensing: The role of the building block in multiscale SERS substrates. *Adv. Funct. Mater.* **2010**, *20*, 2619–2628.

[10] Chen, P. C.; Liu, X. L.; Hedrick, J. L.; Xie, Z.; Wang, S. Z.; Lin, Q. Y.; Hersam, M. C.; Dravid, V. P.; Mirkin, C. A. Polyelemental nanoparticle libraries. *Science* **2016**, *352*, 1565–1569.

[11] Chen, P. C.; Liu, G. L.; Zhou, Y.; Brown, K. A.; Chernyak, N.; Hedrick, J. L.; He, S.; Xie, Z.; Lin, Q. Y.; Dravid, V. P. et al. Tip-directed synthesis of multimetallic nanoparticles. *J. Am. Chem. Soc.* **2015**, *137*, 9167–9173.

[12] Gargiulo, J.; Violi, I. L.; Cerrota, S.; Chvátal, L.; Cortés, E.; Perassi, E. M.; Diaz, F.; Zemánek, P.; Stefani, F. D. Accuracy and mechanistic details of optical printing of single Au and Ag nanoparticles. *ACS Nano* **2017**, *11*, 9678–9688.

[13] Zhang, H. Y.; Cadusch, J.; Kinnear, C.; James, T.; Roberts, A.; Mulvaney, P. Direct assembly of large area nanoparticle arrays. *ACS Nano* **2018**, *12*, 7529–7537.

[14] Hong, X.; Tan, C. L.; Chen, J. Z.; Xu, Z. C.; Zhang, H. Synthesis, properties and applications of one- and two-dimensional gold nanostructures. *Nano Res.* **2015**, *8*, 40–55.

[15] Chen, Y.; Fan, Z. X.; Zhang, Z. C.; Niu, W. X.; Li, C. L.; Yang, N. L.; Chen, B.; Zhang, H. Two-dimensional metal nanomaterials: Synthesis, properties, and applications. *Chem. Rev.* **2018**, *118*, 6409–6455.

[16] Golze, S. D.; Hughes, R. A.; Rouvimov, S.; Neal, R. D.; Demille, T. B.; Neretina, S. Plasmon-mediated synthesis of periodic arrays of gold nanoplates using substrate-immobilized seeds lined with planar defects. *Nano Lett.* **2019**, *19*, 5653–5660.

[17] Yoo, Y.; Kim, S. I.; Kim, J.; Kim, B. Geometry-tailored freestanding epitaxial Pd, AuPd, and Au nanoplates driven by surface interactions. *Nanoscale* **2020**, *12*, 6537–6544.

[18] Yoo, Y.; Lee, H.; Lee, H.; Lee, M.; Yang, S.; Hwang, A.; Kim, S. I.; Park, J. Y.; Choo, J.; Kang, T. et al. Surfactant-free vapor-phase synthesis of single-crystalline gold nanoplates for optimally bioactive surfaces. *Chem. Mater.* **2017**, *29*, 8747–8756.

[19] Sun, Y. G. Metal nanoplates on semiconductor substrates. *Adv. Funct. Mater.* **2010**, *20*, 3646–3657.

[20] Wu, Q. Y.; Diao, P.; Sun, J.; Jin, T.; Xu, D.; Xiang, M. Electrodeposition of vertically aligned silver nanoplate arrays on indium tin oxide substrates. *J. Phys. Chem. C* **2015**, *119*, 20709–20720.

[21] Seo, B.; Choi, S.; Kim, J. Simple electrochemical deposition of Au nanoplates from Au(I) cyanide complexes and their electrocatalytic activities. *ACS Appl. Mater. Interfaces* **2011**, *3*, 441–446.

[22] Scarabelli, L.; Coronado-Puchau, M.; Giner-Casares, J. J.; Langer, J.; Liz-Marzán, L. M. Monodisperse gold nanotriangles: Size control, large-scale self-assembly, and performance in surface-enhanced Raman scattering. *ACS Nano* **2014**, *8*, 5833–5842.

[23] Lee, Y. H.; Lee, C. K.; Tan, B. R.; Rui Tan, J. M.; Phang, I. Y.; Ling, X. Y. Using the Langmuir–Schaefer technique to fabricate large-area dense SERS-active Au nanoprism monolayer films. *Nanoscale* **2013**, *5*, 6404–6412.

[24] Liebig, F.; Sarhan, R. M.; Prietzel, C.; Reinecke, A.; Koetz, J. "Green" gold nanotriangles: Synthesis, purification by polyelectrolyte/micelle depletion flocculation and performance in surface-enhanced Raman scattering. *RSC Adv.* **2016**, *6*, 33561–33568.

[25] Fu, Q.; Ran, G. J.; Xu, W. L. Direct self-assembly of CTAB-capped Au nanotriangles. *Nano Res.* **2016**, *9*, 3247–3256.

[26] Liyanage, T.; Masterson, A. N.; Hati, S.; Ren, G.; Manicke, N. E.; Rusyniak, D. E.; Sardar, R. Optimization of electromagnetic hot spots in surface-enhanced Raman scattering substrates for an ultrasensitive drug assay of emergency department patients' plasma. *Analyst* **2020**, *145*, 7662–7672.

[27] Walker, D. A.; Browne, K. P.; Kowalczyk, B.; Grzybowski, B. A. Self-assembly of nanotriangle superlattices facilitated by repulsive electrostatic interactions. *Angew. Chem.* **2010**, *122*, 6912–6915.

[28] Zhou, Y.; Zhou, X. Z.; Park, D. J.; Torabi, K.; Brown, K. A.; Jones, M. R.; Zhang, C.; Schatz, G. C.; Mirkin, C. A. Shape-selective deposition and assembly of anisotropic nanoparticles. *Nano Lett.* **2014**, *14*, 2157–2161.

[29] Beeram, S. R.; Zamborini, F. P. Purification of gold nanoplates grown directly on surfaces for enhanced localized surface plasmon resonance biosensing. *ACS Nano* **2010**, *4*, 3633–3646.

[30] Zhang, X. Y.; Hu, A. M.; Zhang, T.; Lei, W.; Xue, X. J.; Zhou, Y. H.; Duley, W. W. Self-assembly of large-scale and ultrathin silver nanoplate films with tunable Plasmon resonance properties. *ACS Nano* **2011**, *5*, 9082–9092.

[31] Liyanage, T.; Rael, A.; Shaffer, S.; Zaidi, S.; Goodpaster, J. V; Sardar, R. Fabrication of a self-assembled and flexible SERS nanosensor for explosive detection at parts-per-quadrillion levels from fingerprints. *Analyst* **2018**, *143*, 2012–2022.

[32] Liyanage, T.; Masterson, A. N.; Oyem, H. H.; Kaimakliotis, H.; Nguyen, H.; Sardar, R. Plasmoelectronic-based ultrasensitive assay of tumor suppressor microRNAs directly in patient plasma: Design of highly specific early cancer diagnostic technology. *Anal. Chem.* **2019**, *91*, 1894–1903.

[33] Hwang, A.; Kim, E.; Moon, J.; Lee, H.; Lee, M., Jeong, J.; Lim, E. K.; Jung, J.; Kang, T.; Kim, B. Atomically flat Au nanoplate platforms enable ultraspecific attomolar detection of protein biomarkers. *ACS Appl. Mater. Interfaces* **2019**, *11*, 18960–18967.

[34] Yang, S.; Park, K.; Kim, B.; Kang, T. Low-temperature vapor-phase synthesis of single-crystalline gold nanostructures: Toward exceptional electrocatalytic activity for methanol oxidation reaction. *Nanomaterials* **2019**, *9*, 595.

[35] Li, Y. Y.; Diao, P.; Jin, T.; Sun, J.; Xu, D. Shape-controlled electrodeposition of standing Rh nanoplates on indium tin oxide substrates and their electrocatalytic activity toward formic acid oxidation. *Electrochim. Acta* **2012**, *83*, 146–154.

[36] Jeong, W.; Lee, M.; Lee, H.; Lee, H.; Kim, B.; Park, J. Y. Ultraflat Au nanoplates as a new building block for molecular electronics. *Nanotechnology* **2016**, *27*, 215601.

[37] Menumerov, E.; Golze, S. D.; Hughes, R. A; Neretina, S. Arrays of highly complex noble metal nanostructures using nanoimprint lithography in combination with liquid-phase epitaxy. *Nanoscale* **2018**, *10*, 18186–18194.

[38] Tan, T. X.; Zhang, S.; Wang, J.; Zheng, Y. Q.; Lai, H. P.; Liu, J. L.; Qin, F. Q.; Wang, C. Resolving the stacking fault structure of silver nanoplates. *Nanoscale* **2021**, *13*, 195–205.

[39] Xia, Y. N.; Gilroy, K. D.; Peng, H. C.; Xia, X. H. Seed-mediated growth of colloidal metal nanocrystals. *Angew. Chem., Int. Ed.* **2017**, *56*, 60–95.

[40] Farzinpour, P.; Sundar, A.; Gilroy, K. D.; Eskin, Z. E.; Hughes, R. A.; Neretina, S. Dynamic templating: A large area processing route for the assembly of periodic arrays of sub-micrometer and nanoscale structures. *Nanoscale* **2013**, *5*, 1929–1938.

[41] Jang, M. H.; Kim, J. K.; Tak, H.; Yoo, H. Controllable synthesis of multi-layered gold spirangles. *J. Mater. Chem.* **2011**, *21*, 17606–17608.

[42] Oh, J. H.; Lee, J. S. One-pot photochemical synthesis of gold nanoplates using nonionic diblock copolymers and their surface functionalization. *Bull. Korean Chem. Soc.* **2018**, *39*, 1165–1170.

[43] Sun, Z. W.; Chen, X.; Wang, L. Y.; Zhang, G. D.; Jing, B. Synthesis of gold nanoplates in lamellar liquid crystal. *Colloids Surf. A: Physicochem. Eng. Asp.* **2008**, *326*, 23–28.

[44] Kim, B. H.; Oh, J. H.; Han, S. H.; Yun, Y. J.; Lee, J. S. Combinatorial polymer library approach for the synthesis of silver nanoplates. *Chem. Mater.* **2012**, *24*, 4424–4433.

[45] Bialas, H.; Heneka, K. Epitaxy of fcc metals on dielectric substrates. *Vacuum* **1994**, *45*, 79–87.

[46] Jauffred, L.; Samadi, A.; Klingberg, H.; Bendix, P. M.; Oddershede, L. B. Plasmonic heating of nanostructures. *Chem. Rev.* **2019**, *119*, 8087–8130.

[47] Joshi, G. K.; McClory, P. J.; Muhoberac, B. B.; Kumbhar, A.; Smith, K. A.; Sardar, R. Designing efficient localized surface Plasmon resonance-based sensing platforms: Optimization of sensor response by controlling the edge length of gold nanoprisms. *J. Phys. Chem. C* **2012**, *116*, 20990–21000.

[48] Beeram, S. R.; Zamborini, F. P. Selective attachment of antibodies to the edges of gold nanostructures for enhanced localized surface Plasmon resonance biosensing. *J. Am. Chem. Soc.* **2009**, *131*, 11689–11691.

[49] Jiang, T.; Wang, X. L.; Tang, J.; Tang, S. W. Seed-mediated synthesis of floriated Ag nanoplates as surface enhanced Raman scattering substrate for in situ molecular detection. *Mater. Res. Bull.*, **2018**, *97*, 201–206.

[50] Schweitz, K. O.; Schou-Jensen, R. B.; Eskildse, S. S. Ultrasonic pre-treatment for enhanced diamond nucleation. *Diam. Relat. Mater.* **1996**, *5*, 206–210.

[51] Rodriguez-Navarro, A. B. *XRD2DScan*: New software for polycrystalline materials characterization using two-dimensional X-ray diffraction. *J. Appl. Crystallogr.* **2006**, *39*, 905–909.